Science Bulletin 70 (2025) 951–959

Contents lists available at ScienceDirect

Science Bulletin

journal homepage: www.elsevier.com/locate/scib

Article

Shortwave cloud warming effect observed over highly reflective Greenland

Haotian Zhang [a], Chuanfeng Zhao [a,b,*], Jing Li [a], Yan Yu [a], Annan Chen [a], Yikun Yang [a], Yan Xia [c], Jie Yang [d], Yue Sun [e], Yulei Chi [d], Xin Zhao [d], Yuan Wang [f], Jianping Huang [g]

[a] Department of Atmospheric and Oceanic Sciences, School of Physics, Peking University, Beijing 100871, China
[b] Institute of Carbon Neutrality, Peking University, Beijing 100871, China
[c] School of Systems Science, Beijing Normal University, Beijing 100875, China
[d] Faculty of Geographical Science, Beijing Normal University, Beijing 100875, China
[e] School of Atmospheric Physics, Nanjing University of Information Science & Technology, Nanjing 210044, China
[f] Department of Earth System Science, Stanford University, Palo Alto, CA 94305, USA
[g] Key Laboratory for Semi-Arid Climate Change of the Ministry of Education, College of Atmospheric Sciences, Lanzhou University, Lanzhou 730000, China

ARTICLE INFO

Article history:
Received 19 August 2024
Received in revised form 29 December 2024
Accepted 30 December 2024
Available online 16 January 2025

Keywords:
Cloud
Cloud radiative effect
Greenland
Earth's energy budget

ABSTRACT

Clouds significantly influence the Earth's energy budget, typically exerting a net global cooling effect by balancing shortwave radiation shading and longwave radiation trapping. However, here we report a shortwave warming effect by clouds over Greenland, contrary to the conventional belief of a cooling effect. We find that the shortwave cloud warming effect on the Earth-atmosphere system is particularly prominent for optically thin clouds. Utilizing satellite-based observations over Greenland during the summer season from 2013 to 2022, we identify a positive shortwave cloud radiative effect when the ratio of surface albedo to top-of-atmosphere (TOA) reflectivity reaches a critical threshold, implying that cloud-induced warming can occur in any place when the surface is bright enough compared with TOA. The shortwave warming effect (with radiative effect up to 25 W/m^2) over Greenland is primarily concentrated in the peripheries and southern margins—regions experiencing the most intense ice melt. From a global perspective, these warming clouds can contribute up to 0.36 W/m^2 to the summer Earth-atmosphere system in the Northern Hemisphere. These findings are critical for understanding the radiation budget in the polar regions, improving predictions of polar ice melt, and enhancing our comprehension of the Earth's energy budget.

1. Introduction

Clouds regulate the energy balance of the Earth-atmosphere system through the intricate interplay of shortwave radiation shading and longwave radiation trapping [1–3]. As global warming intensifies and extreme weather events become more frequent, understanding the radiative effect mechanisms of clouds within the Earth-atmosphere system has emerged as a central focus of climate research. This focus is particularly pronounced in polar regions, where the cloud radiative effect (CRE) assumes a pivotal role in shaping the freeze-thaw dynamics of polar land and sea ice, which is closely linked to polar climate change [4–7].

The behavior of polar CREs is contingent upon a triad of factors: surface albedo (α), cloud properties, and solar zenith angle (SZA) [8]. Among these factors, the Greenland ice sheet (GrIS) and its encompassing milieu stand out as a Northern Hemispheric high-latitude region acutely sensitive to climate change, intricately entwined with various facets of the global climate system [9–13]. Over the past two decades, the GrIS has witnessed a markedly accelerated ice loss attributed to rising temperatures, significantly outpacing the rates predicted by prevailing models [14,15]. This acceleration, coupled with the increasing global warming and heightened extreme climatic events, has propelled the climate of Greenland into the forefront of ongoing climate investigations [16–19].

Distinctive attributes mark the CRE over the GrIS, diverging from those observed in the broader Arctic context. In many instances, the net CRE at the surface yields a warming effect,

* Corresponding author.
E-mail address: cfzhao@pku.edu.cn (C. Zhao).

https://doi.org/10.1016/j.scib.2025.01.027

particularly pronounced during winter and spring [20,21]. Cloud properties, particularly the cloud optical depth (COD), play a critical role in determining CRE [22,23]. While thin clouds exhibit a subdued albedo effect in the Arctic, their robust longwave-warming influence magnifies the net warming effect at the surface [24–27]. A notable instance from July 2012, documented at the Summit Ground-based Observatory in Greenland, underscores that low-altitude clouds can elevate surface temperatures beyond the melting point of snow, inducing surface melt. This surface melt, in turn, diminishes surface albedo, augmenting solar radiation absorption, thereby perpetuating changes in cloud-induced radiative effect [25]. The warming effect attributed to clouds over the GrIS results from the interplay of shortwave cloud radiative effect (SWCRE) and longwave cloud radiative effect (LWCRE), wherein the warming impact of LWCRE outweighs the cooling effect of SWCRE [28]. Compared with surface radiative effects, research on top-of-atmosphere (TOA) CREs has largely focused on the entire Arctic region. Many studies have quantified the contributions of the atmosphere and surface to changes in TOA shortwave radiative effects. In the Arctic, the contribution of TOA shortwave radiative effects to the energy balance of the entire climate system is highly dependent on the TOA SWCRE [29,30]. Meanwhile, changes in surface sea ice and snow cover can also influence the TOA SWCRE [31,32]. However, previous studies have primarily focused on the annual mean, multi-year summer averages, and interannual variations of TOA SWCRE across the entire Arctic, with few exploring the deeper physical mechanisms of changes in TOA SWCRE over high-albedo surfaces [31–35].

In this study, we unveil that over high albedo terrains, TOA SWCRE can result in warming effects, particularly when thin clouds are in play. This warming effect, however, is intricately modulated by cloud properties and SZA. Chen et al. [36] explored the impact of the TOA aerosol warming effect (AWE) and examined how surface albedo variations influence AWE. However, previous studies have rarely addressed the mechanism of cloud-induced TOA SWCRE warming over high-albedo surfaces. Our primary focus rests on investigating the impact of COD on SWCRE, evaluating the variability of SWCRE with SZA across distinct surface albedo-to-TOA reflectance ratios, and calculating the global effect of cloud-induced shortwave warming.

2. Materials and methods

2.1. CERES-SSF orbital dataset

This study uses the Clouds and the Earth's Radiant Energy System (CERES) Single Scanner Footprint (SSF) dataset, including surface albedo, SZA, mean visible optical depth for cloud layer, TOA incoming solar radiation and TOA upwards shortwave radiation (Aqua satellite). Both the TOA incoming solar radiation and TOA upward shortwave radiation data are directly based on observations. CERES-SSF measures the upward radiance at TOA in three spectral bands. By using Angular Distribution Models (ADMs) upward fluxes can be well estimated [37]. As we focus on the shortwave radiative effect of clouds, we have only considered the daytime situation, when TOA incoming solar radiation is greater than 0.

2.2. SYN1deg dataset

The SYN1deg dataset provides monthly mean radiative fluxes and cloud properties on a global by 1°×1° grid. This dataset integrates measurements from MODIS (Moderate Resolution Imaging Spectroradiometer) sensor and GEO (Geostationary Operational Environmental Satellite) systems, offering comprehensive coverage of cloud properties and radiation data [38]. The SYN1deg data is used in this study to cross-validate the CERES-SSF findings, providing a broader context and confirming the consistency of the observed SWCRE warming effect.

2.3. Surface Albedo dataset

The CERES Synoptic (SYN1deg) product provides high-quality global surface albedo data on hourly and monthly basis at a 1°×1° spatial resolution. These surface albedo values are derived using the Langley-modified Fu-Liou Radiative Transfer Model (RTM) based on inputs from Terra and Aqua MODIS data, 3-h geostationary (GEO) satellite observations, and meteorological assimilation data from the Goddard Earth Observing System Version 5.4.1 [39]. This integration of satellite and meteorological data allows for accurate estimation of surface albedo across different geographic regions and time scales, supporting its use in radiative flux calculations in the atmosphere and at the surface.

To better assess and validate the accuracy of surface albedo data from the CERES albedo product, we use the surface albedo data from the "AVHRR Polar Pathfinder (APP) and Extended AVHRR Polar Pathfinder (APP-x) Climate Data Records, Version 1" dataset provided by the National Snow and Ice Data Center (NSIDC) [40]. APP is a fundamental Climate Data Record (CDR) that provides channel reflectance and brightness temperatures from twice-daily observations spanning the period from 1982 to the present for the polar region.

2.4. Calculating CRE

Our general approach for investigating the CREs from satellite observations is outlined here. Since we use the mean visible optical depth for cloud layer variable from CERES-SSF dataset, clouds are considered to be present when the COD of a single cloud layer is greater than 0. The SWCRE involved in this study is divided into two types. One for the SWCRE in Section 3.1, which is defined as the difference between cloudy-sky and clear-sky TOA radiative fluxes. We calculate the SWCRE using Eqs. (1) and (2):

$$\mathrm{NetSW} = \mathrm{DSW} - \mathrm{USW}, \tag{1}$$

$$\mathrm{SWCRE}^1{}_{\mathrm{full-cloud}} = \mathrm{NetSW}^1{}_{\mathrm{cloudy-sky}} - \mathrm{NetSW}^1{}_{\mathrm{clear-sky}}, \tag{2}$$

where DSW and USW denote downward and upward shortwave radiations, respectively; NetSW represents the net shortwave radiation. The $\mathrm{SWCRE}^1_{\mathrm{full\text{-}cloud}}$ is considered as the TOA CRE with a cloud fraction of 100% (as shown in Section 3.1) based on CERES-SSF dataset. The other one is the two-dimensional average SWCRE, which is calculated based on SYN1deg dataset as Eqs. (1) and (3):

$$\mathrm{SWCRE}^2 = \mathrm{NetSW}^2{}_{\mathrm{all-sky}} - \mathrm{NetSW}^2{}_{\mathrm{clear-sky}}, \tag{3}$$

where SWCRE^2 represents the monthly average shortwave CRE calculated using the SYN1deg dataset, which is also influenced by the cloud fraction (unlike $\mathrm{SWCRE}^1_{\mathrm{full\text{-}cloud}}$ that assumes a cloud fraction of 100%). SWCRE^2 is used to assess the long-term and large-scale average effects of cloud-induced radiative effects, as shown in Section 3.2. The calculation formulas for LWCRE and net cloud radiative effect (NETCRE) presented in Section 3.2 are provided in Eqs. (4)–(7):

$$\mathrm{NetLW} = \mathrm{DLW} - \mathrm{ULW}, \tag{4}$$

$$\mathrm{NetRad} = \mathrm{NetLW} + \mathrm{NetSW}, \tag{5}$$

$$\mathrm{LWCRE} = \mathrm{NetLW}_{\mathrm{all-sky}} - \mathrm{NetLW}_{\mathrm{clear-sky}}, \tag{6}$$

$$\mathrm{NETCRE} = \mathrm{NetRad}_{\mathrm{all-sky}} - \mathrm{NetRad}_{\mathrm{clear-sky}}, \tag{7}$$

where DLW and ULW represent the downward and upward longwave radiations, respectively; NetLW and NetRad respectively represent the net shortwave radiation and net radiation. We also define the downward radiation at TOA as positive.

2.5. Defining $R_{S/T}$: a conceptual overview

In the scenario discussed here, the path of shortwave solar radiation through the atmosphere and surface can be depicted using a single-layer solar radiation model [41]. This model primarily considers three shortwave processes: atmospheric reflection, atmospheric absorption, and surface reflection. A key theoretical aspect highlighted is the multiple reflections of shortwave radiation between the cloud base and the surface. During this process, a portion of the shortwave radiation is absorbed by the surface, another portion by the atmosphere, and the remainder traverses the atmosphere to escape into space. The resultant upward shortwave radiative flux at the top of the atmosphere is quantified as:

$$\begin{aligned}\mathrm{USW}_{\mathrm{TOA}} = {} & S\Big[R + \alpha(1-R-A)^2 + \alpha^2 R(1-R-A)^2 \\ & + \alpha^3 R^2 (1-R-A)^2 \cdots\Big] \\ = {} & SR + S\alpha(1-R-A)^2\Big[1 + (\alpha R) + (\alpha R)^2 \cdots\Big] \\ = {} & SR + S\alpha\frac{(1-R-A)^2}{1-\alpha R},\end{aligned} \tag{8}$$

where S represents the incident solar shortwave radiation, while A, R, and α denote the atmospheric absorption fraction during a single pass through the atmosphere, the fraction of cloud reflection, and the surface albedo, respectively. We assume that S and A are constant, or that variations $\mathrm{USW}_{\mathrm{TOA}}$ is driven by changes in S and A are negligible compared to other variables. Consequently, $\mathrm{USW}_{\mathrm{TOA}}$ and SWCRE are primarily influenced by R and α. When the sky is fully clouded (i.e., cloud fraction is 100%), R is principally related to the optical depth of the clouds. Therefore, we define a new parameter, $R_{S/T}$, to characterize the variation in $\mathrm{USW}_{\mathrm{TOA}}$, which is given by

$$R_{S/T} = \text{Surface albedo}\,(\alpha)/\text{TOA reflectance}(\sim R), \tag{9}$$

$$\text{TOA reflectance} = \text{USW}/\text{DSW}. \tag{10}$$

$R_{S/T}$ is a dimensionless parameter that reflects changes in both α and R, capturing their combined influence on $\mathrm{USW}_{\mathrm{TOA}}$, making it an effective metric for assessing the shortwave cloud radiative warming effect. We utilize Santa Barbara DISORT Atmospheric Radiative Transfer (SBDART) model [42] to simulate CRE and $R_{S/T}$ across a range of COD and surface albedo conditions, with results indicating the presence of a shortwave warming effect (Text S2; Fig. S1 online). Notably, the CERES-SSF and SYN1deg datasets contain inherent uncertainties over snow and ice surfaces [43]. Nevertheless, these uncertainties do not alter our conclusion that lower COD values are associated with an increased likelihood of cloud-induced shortwave warming over high-albedo surfaces (refer to Section 3.1). In calculating TOA reflectance, only the observed parameters USW and DSW are utilized (Eq. (10)), effectively avoiding the potential for deviations stemming from COD measurement errors.

In addition, CERES-SSF data divides the observed clouds into two layers: Layer-1 and Layer-2, and only single-layer clouds are considered in this study, i.e., the case of Layer-2 is with a COD of 0. We grid the single-layer clouds and clear-sky cases observed during summer from 2013 to 2022 in the study area by latitude and longitude in two dimensions. Notably, for the sake of clarity and intuitive analysis, our study exclusively encompasses single-layer cloud scenarios, omitting considerations of double-layer or multi-layer cloud conditions in Section 3.1.

In contrast to the instantaneous $R_{S/T}$ calculated in Section 3.1 to explore the principles underlying the SWCRE warming effects, the $R_{S/T}$ calculation in Section 3.2 is adjusted to align with the analysis of monthly-averaged SWCRE warming effects. This adjustment utilizes SYN1deg data for the monthly average surface albedo and TOA reflectance. This approach accounts for various cloud layers and SZAs, providing a long-term average $R_{S/T}$. Unlike the instantaneous $R_{S/T}$ in Section 3.1, which focuses on the principle of SWCRE warming effects, this calculation emphasizes a time-averaged perspective on surface-cloud interactions, providing insights into their broader, global impact.

2.6. Discussion of uncertainties

Upon introducing $R_{S/T}$ as a threshold measure for assessing the shortwave radiative effects of clouds at TOA, two primary sources of uncertainty emerge. The first is the error in surface albedo retrieval from the CERES data product. The second pertains to errors in surface albedo under all-sky and clear-sky scenarios when calculating CREs at different $R_{S/T}$ values using CERES data. We utilize the surface albedo product APP-x provided by the NSIDC for the summer months from 2013 to 2022 to assess the discrepancies in surface albedo data across all scenarios compared to the CERES albedo data (Fig. S2 online). Additionally, we compare the differences in surface albedo between all-sky and clear-sky conditions as provided by CERES. Fig. S2a (online) shows a scatter plot of the average values within the study area, with a spatial resolution of 1°×1°. The correlation coefficient between the two datasets is high, at 0.96, indicating strong agreement. However, the consistency decreases somewhat in scenarios involving highly reflective surfaces. As shown in Fig. S2 (online), the mean bias of 0.037 indicates that the albedo values from the CERES product are higher than those from the APP-x product. This suggests that the $R_{S/T}$ values derived from CERES albedo data may be larger than the actual values. In our SBDART model sensitivity experiments, we calculate an $R_{S/T}$ threshold of 1.3 (Text S2; Fig. S1 online), while the CERES-based statistics in Section 3.1 yield an $R_{S/T}$ threshold of 1.42. The errors associated with using surface albedo in calculating $R_{S/T}$ are within expected ranges and consistent with model predictions. Fig. S2b (online) demonstrates that the surface albedo data derived from CERES exhibit good consistency between all-sky and clear-sky conditions, with a correlation coefficient of 0.98. Although there are some errors that may lead to discrepancies in the calculated $R_{S/T}$ threshold for cloud-induced shortwave warming from the actual values, our primary objective is to demonstrate that cloud-induced shortwave warming can occur anywhere when the surface is bright enough compared with TOA.

We also utilize two additional datasets, ERA5 and SYN1deg, both of which reveal the presence of SWCRE warming effect (Figs. S3–S8 online). The ERA5 dataset assesses SWCRE under different surface albedo and total column water (TCW) conditions in the Greenland region (noting that ERA5 reanalysis does not provide COD data). We observe that SWCRE warming effect occurs under conditions of low TCW and high surface albedo (Fig. S3 online). Additionally, we use the SYN1deg dataset to evaluate monthly SWCRE from 2013 to 2022 across the Greenland region (Section 3.2 and Fig. S4 online), the Tibetan Plateau (Figs. S5 and S6 online), and West Antarctica (Figs. S7 and S8 online). The results consistently show that SWCRE tends to become positive as $R_{S/T}$ increases, indicating the general applicability of the SWCRE warming effect. The SYN1deg monthly data, which include averages under various conditions such as daytime, nighttime, and different cloud fractions, reveal a threshold that differs from the 1.42 value obtained using CERES-SSF data.

3. Results

3.1. Shortwave CRE varies with COD and surface albedo

We utilize data from the CERES-SSF orbital dataset, focusing on the influence of SWCRE on the Earth-atmosphere system over the GrIS and its peripheral domain (60°–82°N, 0°–80°W). To illustrate the SWCRE warming effect, we present a schematic diagram showing distinctive SWCRE patterns across diverse surface types (Fig. 1). When albedo ≤ 0.15 (mostly over the open sea in the study region), the SWCRE on the Earth-atmosphere system is ($a_1 - a_2 - c_1$) (downward direction is positive), a cooling effect. When the albedo ≥ 0.75 (mostly over the GrIS in the study region) and the sky is clear, the ground partially absorbs shortwave radiation and reflects most of the solar shortwave radiation away from the Earth-atmosphere system, which is denoted by b_1. Under a cloudy situation, the cloud top can partially reflect solar shortwave radiation out of the TOA (c_1), the cloud absorbs part of the solar shortwave radiation, and most of the shortwave radiation that reaches the surface (with a small part absorbed by the surface) is reflected back into the atmosphere. Part of this reflected shortwave radiation is absorbed by the cloud, and the other part is reflected back to the surface by the cloud base, and the cycle continues. Only a portion of the shortwave radiation reflected from the surface escapes the Earth-atmosphere system through the clouds (including the shortwave radiation through clouds during the process), and the total amount of shortwave radiation transmitted through clouds is symbolized by b_2. The shortwave radiation reflected from the Earth-atmosphere system is ($- c_1 - b_2$), and the TOA shortwave radiative effect of clouds relative to the clear sky is ($b_1 - c_1 - b_2$). The magnitude of the cloud shortwave radiative effect depends mainly on the surface albedo, the cloud properties, and the SZA. In case the surface albedo is large (large b_1) enough or/and clouds are sufficiently thin (small c_1), the TOA shortwave radiative effect of clouds ($b_1 - c_1 - b_2$) could become positive and play a warming effect.

The optical depth of clouds hinges upon properties encompassing the cloud phase, cloud effective radius, and the liquid/ice water path, delineating the extent of cloud-mediated reflection and transmission of solar shortwave radiation [44–46]. Here, in the context of summer from 2013 to 2022, we investigate SWCRE across varying surface albedos and SZAs, as illustrated in Fig. 2. Our findings unveil a distinct correlation wherein reduced COD corresponds to elevated SWCRE values, signifying a diminishing effect of shortwave cooling (or amplifying warming) induced by clouds. Beyond COD, surface albedo emerges as an influential factor impinging upon SWCRE. Our inquiry spans three discrete surface albedo intervals: exceeding 0.75 (predominantly over the GrIS), ranging between 0.3 and 0.5 (largely over sea ice), and dipping below 0.15 (primarily over open sea expanses). Notably, results demonstrate that over the GrIS, instances of SWCRE surpassing 0 manifest for scenarios marked by low COD, thus underscoring the potential for shortwave CRE to invoke a warming effect on the Earth-atmosphere system under specific conditions (Fig. 2a and d). In comparison to the GrIS, the proportion of observations with SWCRE values exceeding 0, relative to the overall volume of data, exhibits a pronounced decline over sea ice (Fig. 2b and e; Table 1). Furthermore, only a sparse occurrence of instances with SWCRE surpassing 0 is discerned within the open sea expanse (Fig. 2c and f; Table 1). Differential analyses of SWCRE across varying SZAs further illuminate our exploration. Results depict a tendency for SWCRE to approach 0 under elevated SZAs, aligned with reduced incident solar shortwave radiation. However, the proportion of SWCRE values transcending zero exhibits modest fluctuations in tandem with SZA variations (Table 1). This collective elucidation underscores the fundamental sway wielded by COD and surface albedo as pivotal determinants in shaping the sign of SWCRE.

TOA reflectance, particularly on cloudy days, is intertwined with surface albedo and cloud properties [47–49]. COD determines the extent to which clouds attenuate solar shortwave radiation, which in turn affects TOA reflectance. To unravel the nuanced dynamics underpinning the SWCRE warming effect and mitigate potential biases arising from uncertainties in COD data retrieval, we introduce $R_{S/T}$ (surface albedo/TOA reflectance) as an index delineating the interplay of surface albedo and COD. Analyzing the variation of SWCRE with SZA (Fig. 3a–f) across six $R_{S/T}$ intervals, we observe a trend where an increase in $R_{S/T}$ corresponds to an augmentation (or decline) in the warming (or cooling) impact of SWCRE. Notably, when $R_{S/T}$ is below 1.25, the cooling effect of SWCRE predominates, as elucidated by Fig. 3a–d. Within the $R_{S/T}$ range of 1.25 to 2, SWCRE converges towards neutrality (Fig. 3e), while $R_{S/T}$ surpassing 2 engenders a dominant warming influence in SWCRE (Fig. 3f). Concurrently, with rising SZA values, a mild trend toward neutrality emerges for both warming and cooling effects. The frequency distribution of the six $R_{S/T}$ ranges across

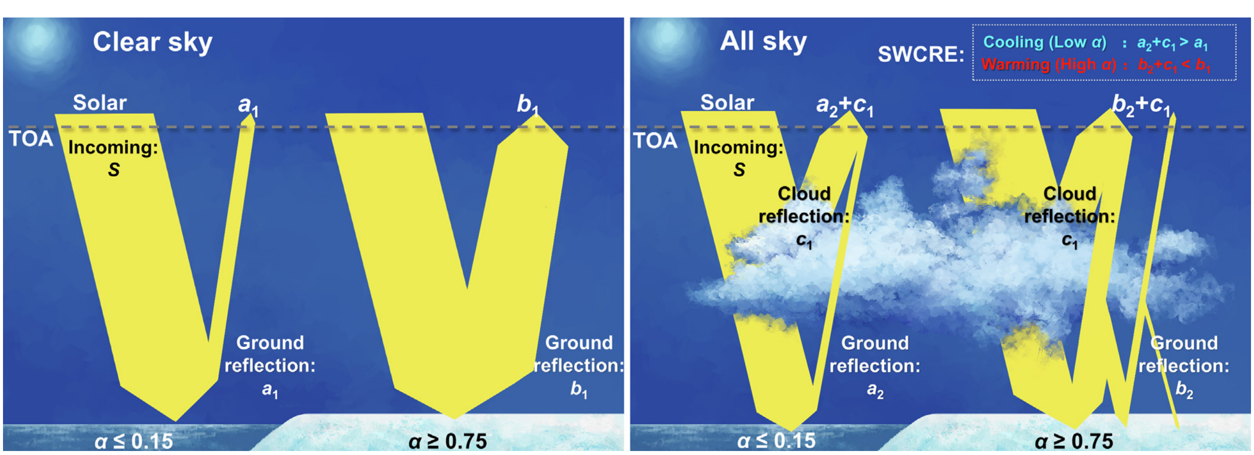

Fig. 1. Schematic illustration of the shortwave radiative cooling and warming effects of clouds over different sub-surfaces. α represents the surface albedo. a_1 denotes solar shortwave radiation reflected from a low-albedo surface under clear sky conditions, while b_1 corresponds to the reflection from a high-albedo surface under clear sky conditions. a_2 represents the reflection from a low-albedo surface under all sky (cloudy) conditions, and b_2 indicates the reflection from a high-albedo surface under all sky conditions, including the radiation transmitted through clouds. c_1 denotes the solar shortwave radiation reflected from the cloud top under all sky conditions.

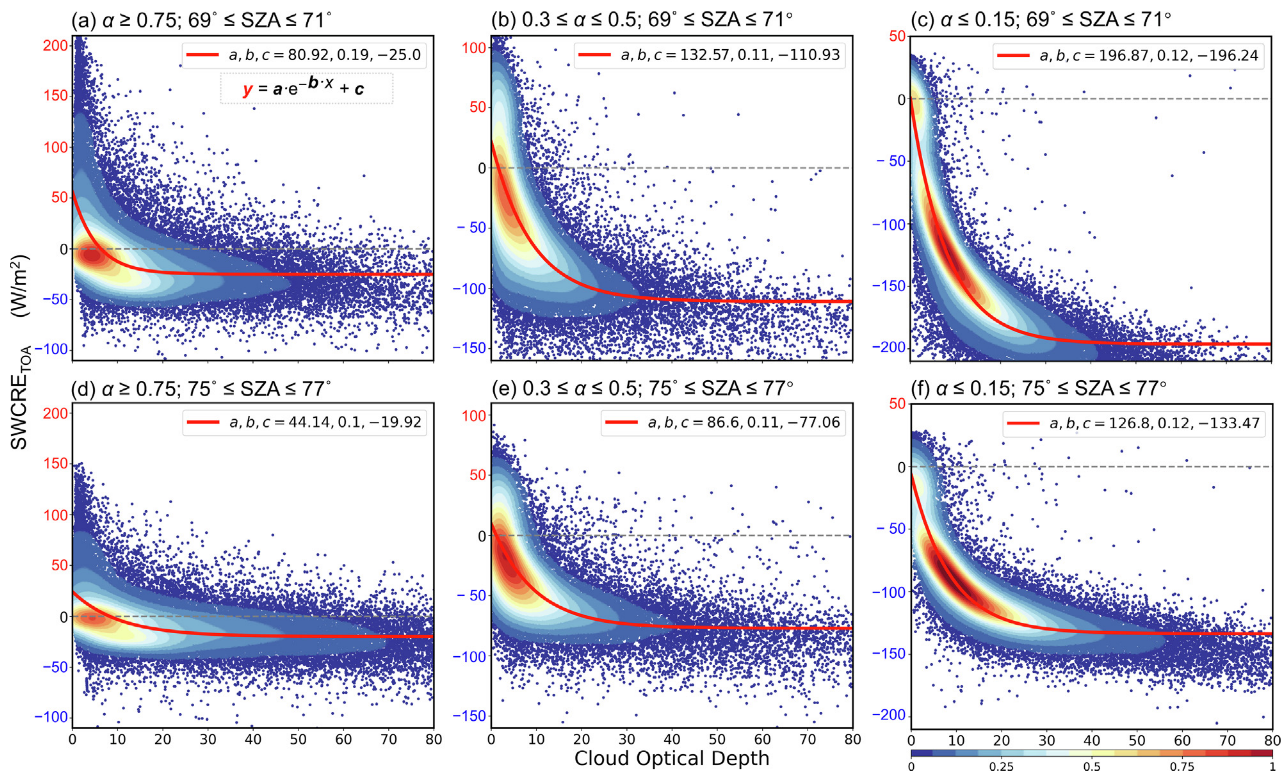

Fig. 2. Variation of the TOA SWCRE with cloud optical depth for different surface albedo and SZA situations. Scatterplots of the net TOA SWCRE with the COD for different surface albedo (albedo ≥ 0.75 (a, d); 0.3 ≤ albedo ≤ 0.5 (b, e); albedo ≤ 0.15 (c, f)) and SZA (69° ≤ SZA ≤ 71° (a–c); 75° ≤ SZA ≤ 77° (d–f)) situations. The color of the dots represents the density distribution (color in probability). The red line denotes the results of the exponential fit between COD and SWCRE. The gray dashed lines represent the results for SWCRE = 0. The *a*, *b*, and *c* in the fitting regression for the red line correspond to the three parameters of the exponential formula. The *y*-axis labels are color-coded, with red indicating SWCRE warming and blue indicating SWCRE cooling.

Table 1
The total number of satellite detections for the six cases (Fig. 2a–f), the number of SWCRE greater than 0 (SWCRE warming), and the proportion of the latter.

	Albedo ≥ 0.75		0.3 ≤ Albedo ≤ 0.5		Albedo ≤ 0.15	
	Case A	Case D	Case B	Case E	Case C	Case F
Total number	426132	500956	110719	121716	139591	235492
SWCRE > 0	146857	177215	25296	24482	7878	6585
Proportion (%)	34.46	35.37	22.84	20.11	5.64	2.79

three distinct surface albedo categories within the study area is depicted in Fig. 3i, which aligns with the scenarios presented in Fig. 2. Over the GrIS expanse (indicated by the red star, albedo ≥ 0.75), the $R_{S/T}$ range of 1.25 to 2 ("e") prevails (61.3%), followed by the $R_{S/T}$ range of 1 to 1.25 ("d") (34.6%). The $R_{S/T}$ range of >2 ("f"), which is capable of inducing a warming effect on the Earth-atmosphere system, constitutes 3.8%. Within the sea ice-covered realm (denoted by the orange star, 0.3 ≤ albedo ≤ 0.5), $R_{S/T}$ ranging from 0.5 to 0.8 ("b") dominates (42.3%). Furthermore, $R_{S/T}$ intervals of 0.8–1.0 ("c"), 1.0–1.25 ("d"), and 1.25–2.0 ("e") represent 29.7%, 16.6%, and 9.5%, respectively. In the open sea domain (characterized by the green star, albedo ≤ 0.15), the $R_{S/T}$ range of 0 to 0.5 ("a") commands a resounding presence (97.3%). Intriguingly, a quantitative threshold emerges through a one-dimensional fit of SWCRE to all $R_{S/T}$ values during the summer daytime hours, revealing that $R_{S/T}$ exceeding 1.42 yields SWCRE values surpassing 0 W/m^2, thereby instigating a warming effect (Fig. 3h).

3.2. SWCRE warming over high $R_{S/T}$ region

Our analysis involves the aggregation of clouds into 1°×1° grid boxes across the two-dimensional spatial coordinates defined by latitude and longitude based on SYN1deg cloud data. Fig. 4a unveils the average cloud fraction distribution from 2013 to 2022. The northern region of GrIS exhibits relatively low cloud cover, approximately 40%, while the central-southern region shows higher cloud fractions, reaching up to 75%. In contrast, cloud cover over maritime regions such as Baffin Bay and the Greenland Sea is notably higher, around 85%–90%. Regarding SWCRE, values exceeding zero are prevalent along the peripheries of Greenland, indicating an overall warming effect, while SWCRE is generally negative over the Greenland Sea and central-southern Greenland (Fig. 4b). Compared to SWCRE, LWCRE across Greenland consistently exhibits a warming trend, ranging from 10 to 30 W/m^2 (Fig. 4c). The NETCRE further highlights a strong warming effect along the edges of Greenland, driven by the combined influence of the SWCRE warming effect and LWCRE, with values ranging from 15 to 30 W/m^2 (Fig. 4d). To explore the overall impact and spatial distribution of the SWCRE warming effect throughout the year, we classify monthly SWCRE > 0 as $SWCRE_{warming}$ for each grid point. Fig. 4e illustrates the frequency of $SWCRE_{warming}$ occurrences, showing a higher frequency along Greenland's edges, with values ranging from 40%–70%. This pattern is also reflected in the $SWCRE_{warming}$ and $R_{S/T}$ values, where the strongest $SWCRE_{warming}$,

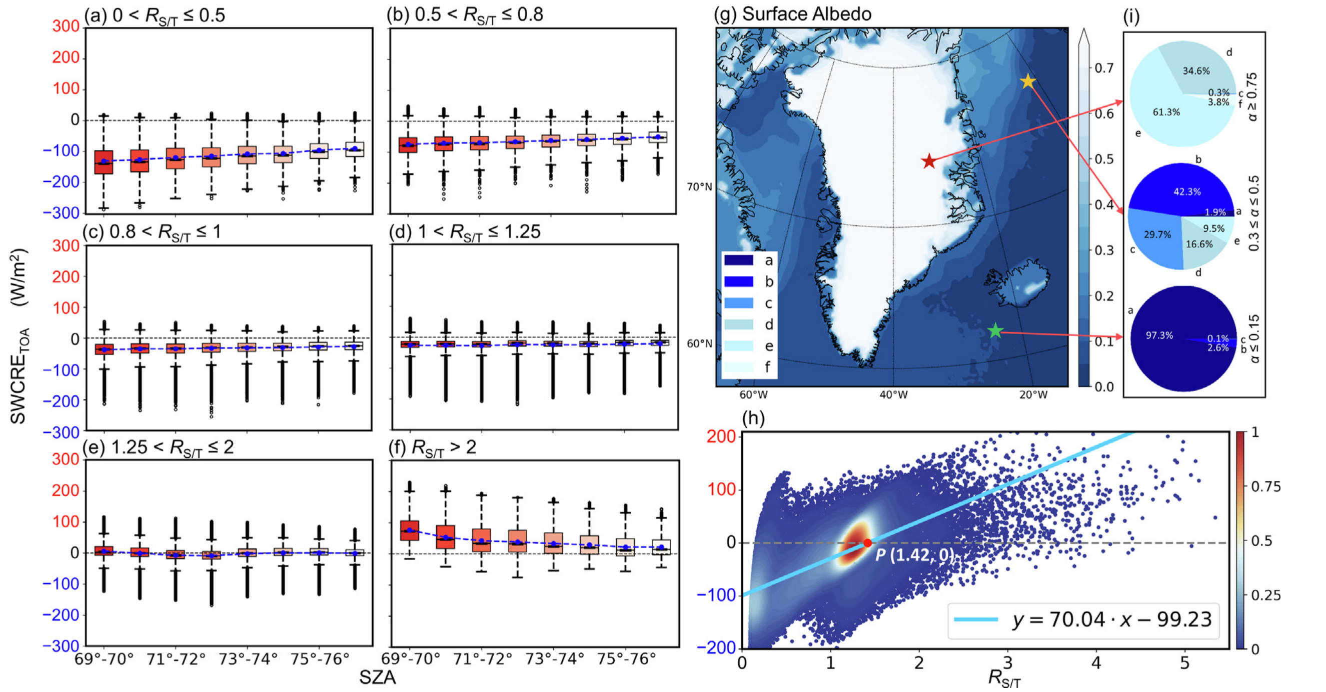

Fig. 3. Variation of SWCRE with SZA for six different $R_{S/T}$ ranges: (a) $0 < R_{S/T} \le 0.5$; (b) $0.5 < R_{S/T} \le 0.8$; (c) $0.8 < R_{S/T} \le 1$; (d) $1 < R_{S/T} \le 1.25$; (e) $1.25 < R_{S/T} \le 2$; (f) $R_{S/T} > 2$. Centre line: median; blue dot: mean; box limits: 25th and 75th percentiles; whiskers: minimum and maximum values that are not considered outliers, that is, 1.5*x* interquartile range. The color gradation of the box indicates the change of SZA (lighter color indicates greater SZA). The *y*-axis labels are color-coded, with red indicating SWCRE warming and blue indicating SWCRE cooling. (g) Map of the study area showing averaged surface albedo during June, July, and August from 2013 to 2022. The labels a–f in the legend box of (g) correspond to the same $R_{S/T}$ ranges as represented in (a–f). (h) Variation of the average SWCRE with different $R_{S/T}$. The blue line corresponds to the slope and intercept in the linear fit formula, while *P* refers to the SWCRE of 0 when $R_{S/T}$ is 1.42. The color of the dots represents the density distribution (color in probability). The gray dashed lines represent the results for SWCRE = 0. (i) The percentage of a–f in three different albedo surfaces (red star, albedo ≥ 0.75; orange star, 0.3 ≤ albedo ≤ 0.5; green star, albedo ≤ 0.15), which corresponds to Fig. 2.

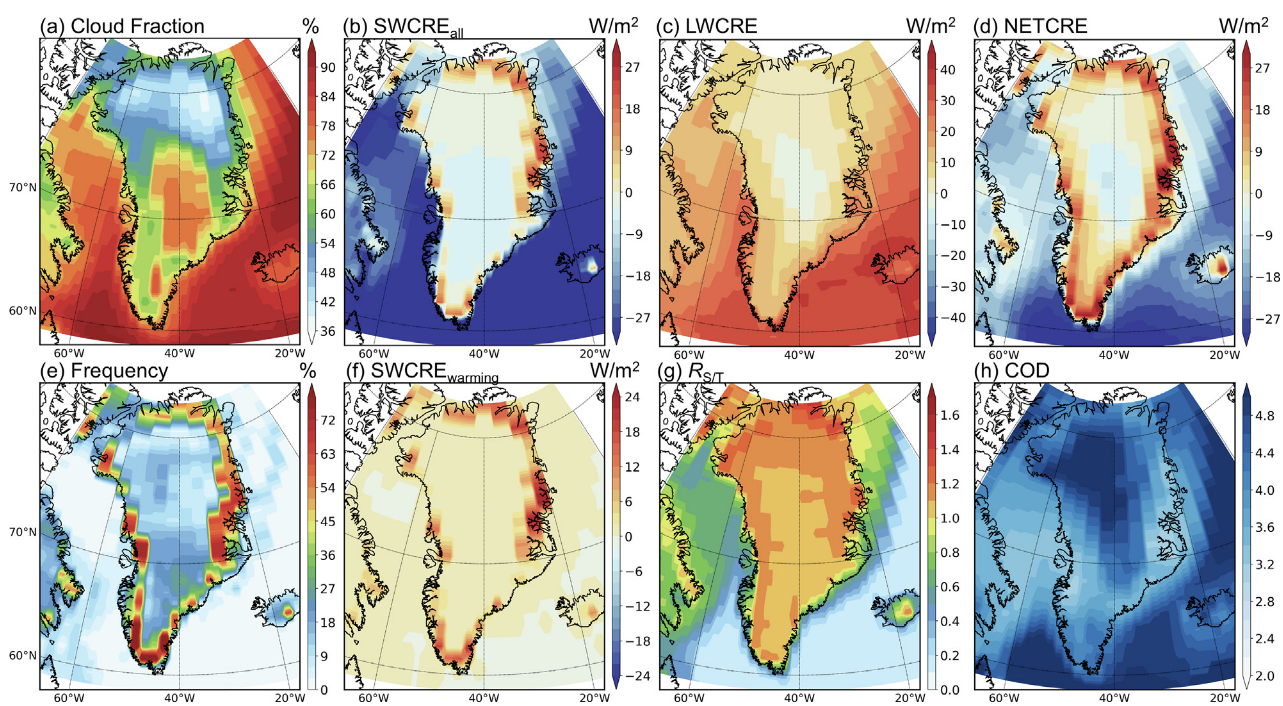

Fig. 4. Spatial distributions of averaged (a) cloud fraction; (b) $SWCRE_{all}$; (c) LWCRE; (d) NETCRE; (e) frequency represents the proportion of $SWCRE_{warming}$ occurrences relative to the $SWCRE_{all}$; (f) $SWCRE_{warming}$; (g) $R_{S/T}$ and (h) COD from 2013 to 2022 in Greenland region.

with an annual average of 10–20 W/m^2, is observed along Greenland's periphery (Fig. 4f). The cloud-fraction-normalized distribution of CREs over Greenland can be found in Fig. S9 (online). Although the cloud fraction in the Greenland region shows notable spatial variability, after normalizing the SWCRF with respect to cloud fraction, the overall trend of cloud radiative warming remains concentrated along the periphery of Greenland. $R_{S/T}$ exhibits pronounced spatial variation, with higher values (ranging from 1.3 to 1.5) observed at Greenland's periphery, differing from the lower values (~1) near the center, and even further reduced values (< 0.5) over the sea (Fig. 4g). The subdued $R_{S/T}$ over the sea is primarily attributed to the diminished surface albedo (Fig. 3g), while the comparatively lower $R_{S/T}$ in central Greenland is mainly due to elevated average COD values (Fig. 4h). Notably, clouds inducing shortwave warming effects are concentrated along Greenland's edges and southern fringes, resulting in a positive radiative effect of 10–20 W/m^2 on the Earth-atmosphere system.

To better observe the impact of the SWCRE warming on the global energy balance, we conduct a quantitative analysis of the global SWCRE warming, including a hemispheric breakdown of its monthly variations (Fig. 5). As shown in Fig. 5b, SWCRE warming is observed globally, with notable findings in Greenland and across other regions, particularly in mid-latitude areas of Asia (with occurrence frequencies of 15%–25%), the Tibetan Plateau (5%–30%) (Fig. S5 online), the Canadian Archipelago (10%–20%), and Antarctica (5%–25%) (Fig. S7 online). Our global quantitative analysis of the SWCRE warming, as shown in Fig. 5c, indicates that shortwave cloud radiative warming occurs in regions such as Antarctica, the Tibetan Plateau, and areas between 30°N and 60°N in Asia and North America, with values ranging from 0.5 to 4.5 W/m^2. Monthly analysis further reveals that $R_{S/T}$ and the SWCRE warming peak in the Northern Hemisphere during March to July, where the SWCRE warming can reach up to 0.36 W/m^2, highlighting its substantial contribution to regional and global warming (Fig. 5d). In the Southern Hemisphere, SWCRE warming averages approximately 0.15 W/m^2 from October to December. $R_{S/T}$ and the SWCRE warming exhibit seasonal variations (Fig. 5d and Fig. S10 online), particularly in the Asian region, which may be related to changes in snowfall and surface albedo. Globally, the SWCRE warming contributes to an average TOA warming of 0.1–0.2 W/m^2. These findings underscore the importance of the SWCRE warming within the global climate system, demonstrating that it contributes to radiative effect across diverse geographical regions. Therefore, accurately accounting for this effect in global climate models is crucial for assessing its impact on the Earth's energy balance and climate dynamics.

4. Conclusion and discussion

Our study reveals the important influence of shortwave cloud radiative warming effect on the Earth-atmosphere system, particularly in high-latitude regions such as the GrIS and its surrounding areas. By analyzing data from the CERES-SSF dataset and SYN1deg dataset (2013–2022), we identify distinct changes in SWCRE associated with varying surface albedos and CODs. Over regions with high surface albedo, such as the GrIS, the SWCRE can induce a warming effect under specific conditions, particularly when COD is low. Additionally, the results indicate that SWCRE warming occurs across various regions globally as long as the surface is highly reflective, including the mid-latitude regions of Asia, the Tibetan Plateau, the Canadian Archipelago, and Antarctica. Our quantitative analysis shows that SWCRE can contribute up to 4.5 W/m^2 of radiative warming in these regions. Seasonal variations in the SWCRE warming are evident, with peaks in the Northern Hemisphere from March to July and in the Southern Hemisphere from October to December. Note that the shortwave warming effect of clouds also occurs even over the extremely low albedo ocean when clouds are sufficiently thin, albeit with a lower probability than over the high albedo surface (Table 1). The $R_{S/T}$ (surface albedo/TOA reflectance) ratio emerges as a key index in understanding the SWCRE impact, revealing that when $R_{S/T}$ reaches a critical threshold, the SWCRE transitions from a

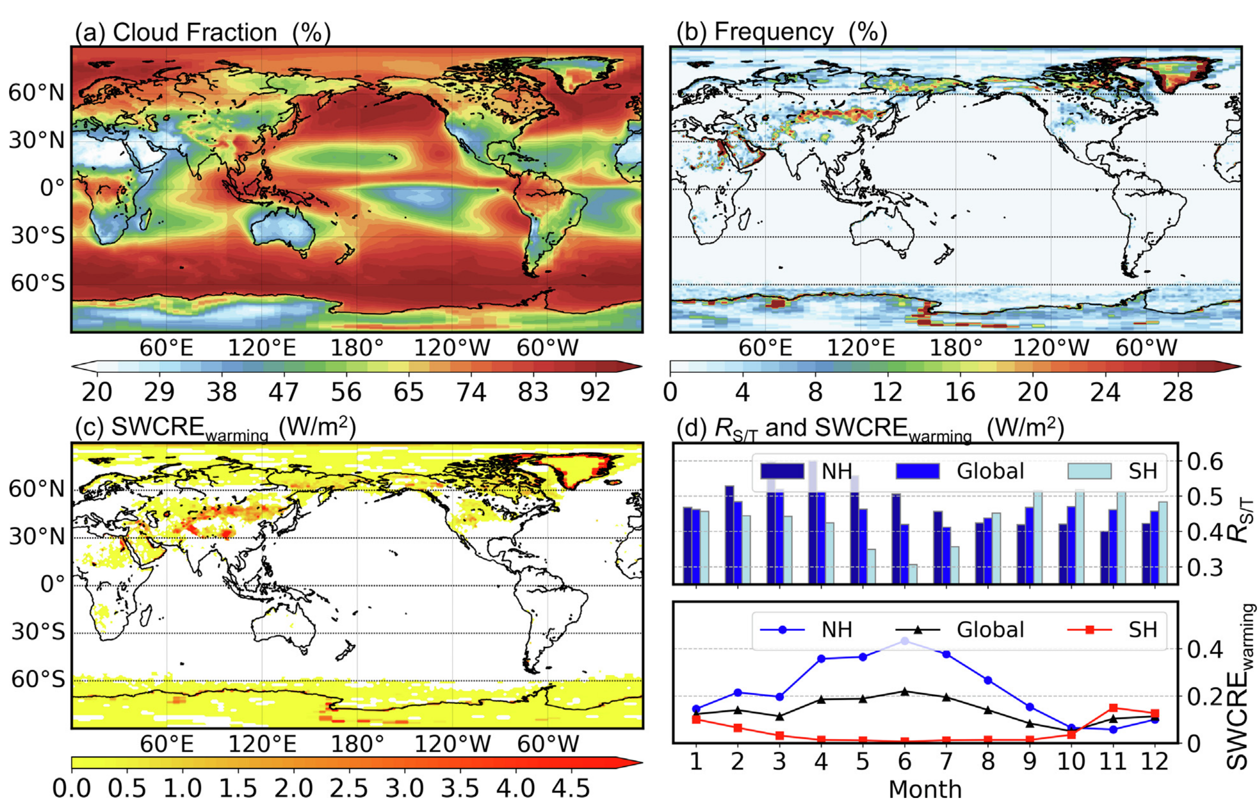

Fig. 5. Spatial distributions of averaged (a) cloud fraction; (b) frequency representing the proportion of $SWCRE_{warming}$ occurrences relative to the $SWCRE_{all}$; and (c) $SWCRE_{warming}$ from 2013 to 2022 for global region. (d) The monthly average of $R_{S/T}$ and $SWCRE_{warming}$ at global and hemispheric scales.

cooling to a warming effect. The spatial distribution and seasonal variation of the SWCRE warming underscore its substantial contribution to regional and global energy balances, particularly in regions with high surface albedo and low COD. Notably, by analyzing historical simulations from seven CMIP6 models and comparing them with CERES observational data and ERA5 reanalysis data, we find that none of the models successfully simulated the SWCRE warming (Table S1 and Fig. S11 online). Although different climate models produce varied results in simulating CREs [50], these findings highlight the critical role of clouds in modulating shortwave radiation and underscore the necessity of incorporating accurate SWCRE representations in global climate models to better assess its impact on the Earth's energy balance and climate dynamics. Furthermore, in accordance with the "snowball Earth" hypothesis, two Neoproterozoic-era global glaciations—the Sturtian glaciation and the Marinoan glaciation—enveloped the planet in ice/snow, accentuating the warming influence of SWCRE and potentially playing a pivotal role in paleo-climate shifts [51–53].

In summation, our satellite-based analyses elucidate that thin clouds can induce a shortwave warming impact on the Earth-atmosphere system above high albedo surfaces, defying the traditional conception of SWCRE primarily instigating cooling effects [54,55]. Our findings unravel part of the intricate interactions between clouds and radiation, providing valuable insights for assessing climate sensitivity and model reliability, thereby enhancing our ability to predict future climate changes. Both the Intergovernmental Panel on Climate Change (IPCC) and the World Climate Research Program (WCRP) underscore the pivotal role of cloud feedback in evaluating climate sensitivity, identifying it as a key source of uncertainty within contemporary climate research [56,57]. In the context of ongoing global warming, comprehending the precise role of surface albedo and clouds within the energy budget of the Earth-atmosphere system has become increasingly important. As global surface albedo continues to decline, vegetation greening in arid regions causes positive radiative forcing [58], while the reduction in the aerosol shortwave radiative warming effect (AWE) partially counteracts the energy increase resulting from albedo reduction [36]. Similarly, the mechanism of SWCRE warming is analogous to that of AWE and may also offset some of the warming in the Earth-atmosphere system caused by decreased surface albedo. Further observational and modeling studies are required to better assess the impact of surface albedo, clouds, and aerosol radiative effects on climate change under future scenarios, which will be the focus of our future research.

Conflict of interest

The authors declare that they have no conflict of interest.

Acknowledgments

This work is supported by the National Natural Science Foundation of China (41925022, 91837204, and 41975023), and the Strategic Priority Research Program of the Chinese Academy of Sciences (XDA19070202). We appreciate Fuzi Huang for support on figure guidance.

Author contributions

Haotian Zhang developed the methodology, carried out the data analysis, interpreted the results, and drafted the manuscript. Chuanfeng Zhao conceived the project, provided supervision, interpreted the results, and edited the manuscript. Jing Li, Yan Yu, Yikun Yang, Yuan Wang, and Jianping Huang assisted with methodology, interpreted the results, and edited the manuscript. Annan Chen, Yan Xia, Jie Yang, Yue Sun, Yulei Chi, and Xin Zhao assisted in data analysis and figure modification. All co-authors contributed to the discussion of the results and provided feedback on the manuscript.

Appendix A. Supplementary material

Supplementary data to this article can be found online at https://doi.org/10.1016/j.scib.2025.01.027.

References

[1] Solomon A, Shupe MD, Miller NB. Cloud-atmospheric boundary layer-surface interactions on the Greenland ice sheet during the July 2012 extreme melt event. J Clim 2017;30:3237–52.
[2] Miller NB, Shupe MD, Lenaerts JTM, et al. Process-based model evaluation using surface energy budget observations in central Greenland. J Geophys Res-Atmos 2018;123:4777–96.
[3] He M, Hu Y, Chen N, et al. High cloud coverage over melted areas dominates the impact of clouds on the albedo feedback in the Arctic. Sci Rep-Uk 2019;9:9511–29.
[4] Hansen J, Sato M, Hearty P, et al. Ice melt, sea level rise and superstorms: evidence from paleoclimate data, climate modeling, and modern observations that 2°C global warming could be dangerous. Atmos Chem Phys 2016;16:3761–812.
[5] Hofer S, Tedstone AJ, Fettweis X, et al. Decreasing cloud cover drives the recent mass loss on the Greenland ice sheet. Sci Adv 2017;3:e1700584.
[6] Muntjewerf L, Sellevold R, Vizcaino M, et al. Accelerated Greenland ice sheet mass loss under high greenhouse gas forcing as simulated by the coupled CESM2.1-CISM2.1. J Adv Model Earth Syst 2020;12:e2019MS002031.
[7] Hanna E, Cappelen J, Fettweis X, et al. Greenland surface air temperature changes from 1981 to 2019 and implications for ice-sheet melt and mass-balance change. Int J Climatol 2021;41:E1336–52.
[8] Sedlar J, Tjernström M, Mauritsen T, et al. A transitioning Arctic surface energy budget: the impacts of solar zenith angle, surface albedo and cloud radiative forcing. Clim Dynam 2011;37:1643–60.
[9] Alexander PM, Tedesco M, Koenig L, et al. Evaluating a regional climate model simulation of Greenland ice sheet snow and firn density for improved surface mass balance estimates. Geophys Res Lett 2019;46:12073–82.
[10] Sherman P, Tziperman E, Deser C, et al. Historical and future roles of internal atmospheric variability in modulating summertime Greenland ice sheet melt. Geophys Res Lett 2020;47:e2019GL086913.
[11] Sjolte J, Adolphi F, Vinther BM, et al. Seasonal reconstructions coupling ice core data and an isotope-enabled climate model: methodological implications of seasonality, climate modes and selection of proxy data. Clim Past 2020;16:1737–58.
[12] Shao Y, Limberg H, Klein K, et al. Human-existence probability of the Aurignacian techno-complex under extreme climate conditions. Quat Sci Rev 2021;263:106995.
[13] Plach A, Vinther BM, Nisancioglu KH, et al. Greenland climate simulations show high Eemian surface melt which could explain reduced total air content in ice cores. Clim Past 2021;17:317–30.
[14] Mernild SH, Mote TL, Liston GE. Greenland ice sheet surface melt extent and trends: 1960–2010. J Glaciol 2011;57:621–8.
[15] Rinke A, Knudsen EM, Mewes D, et al. Arctic summer sea ice melt and related atmospheric conditions in coupled regional climate model simulations and observations. J Geophys Res-Atmos 2019;124:6027–39.
[16] Hay WW. The accelerating rate of global change. Rend Fis Acc Lincei 2014;25:29–48.
[17] Le Clec'H S, Charbit S, Quiquet A, et al. Assessment of the Greenland ice sheet-atmosphere feedbacks for the next century with a regional atmospheric model coupled to an ice sheet model. Cryosphere 2019;13:373–95.
[18] Shannon S, Smith R, Wiltshire A, et al. Global glacier volume projections under high-end climate change scenarios. Cryosphere 2019;13:325–50.
[19] Aoki T, Matoba S, Niwano M, et al. Studies on atmosphere, snow/ice, and glacial microbes on Greenland ice sheet by SIGMA and relevant projects: a linkage to the ArCS II project. J Jpn Soc Snow Ice 2021;83:169–91.
[20] Miller NB, Shupe MD, Cox CJ, et al. Cloud radiative forcing at summit, Greenland. J Clim 2015;28:6267–80.
[21] Van Tricht K, Lhermitte S, Lenaerts JTM, et al. Clouds enhance Greenland ice sheet meltwater runoff. Nat Commun 2016;7:10266.
[22] Ceppi P, Brient F, Zelinka MD, et al. Cloud feedback mechanisms and their representation in global climate models. Clim Change 2017;8:e465.
[23] Terai CR, Klein SA, Zelinka MD, et al. Constraining the low-cloud optical depth feedback at middle and high latitudes using satellite observations. J Geophys Res-Atmos 2016;121:9696–716.
[24] Shupe MD, Intrieri JM. Cloud radiative forcing of the Arctic surface: the influence of cloud properties, surface albedo, and solar zenith angle. J Clim 2004;17:616–28.
[25] Bennartz R, Shupe MD, Turner DD, et al. July 2012 Greenland melt extent enhanced by low-level liquid clouds. Nature 2013;496:83–6.
[26] Zhao C, Garrett TJ. Effects of Arctic haze on surface cloud radiative forcing. Geophys Res Lett 2015;42:557–64.

[27] Miller NB, Shupe MD, Cox CJ, et al. Surface energy budget responses to radiative forcing at Summit, Greenland. Cryosphere 2017;11:497–516.
[28] Zhang H, Zhao C, Xia Y, et al. North Atlantic oscillation-associated variation in cloud phase and cloud radiative forcing over the Greenland Ice Sheet. J Clim 2023;36:3203–15.
[29] Qu X, Hall A. Surface contribution to planetary albedo variability in cryosphere regions. J Clim 2005;18:5239–52.
[30] Sledd A, L'Ecuyer TS. How much do clouds mask the impacts of Arctic sea ice and snow cover variations? different perspectives from observations and reanalyses. Atmosphere 2019;10:12.
[31] Hartmann DL, Ceppi P. Trends in the CERES dataset, 2000–13: the effects of sea ice and jet shifts and comparison to climate models. J Clim 2014;27:2444–56.
[32] Pistone K, Eisenman I, Ramanathan V. Observational determination of albedo decrease caused by vanishing Arctic sea ice. Proc Natl Acad Sci USA 2014;111:3322–6.
[33] Jian B, Li J, Wang G, He Y, Han Y, Zhang M, et al. The impacts of atmospheric and surface parameters on long-term variations in the planetary albedo. J Clim 2018;31:8705–18.
[34] Loeb NG, Wang H, Rose FG, et al. Decomposing shortwave top-of-atmosphere and surface radiative flux variations in terms of surface and atmospheric contributions. J Clim 2019;32:5003–19.
[35] Marcianesi F, Aulicino G, Wadhams P. Arctic sea ice and snow cover albedo variability and trends during the last three decades. Polar Sci 2021;28:100617.
[36] Chen A, Zhao C, Zhang H, et al. Surface albedo regulates aerosol direct climate effect. Nat Commun 2024;15:7816.
[37] Wielicki BA, Barkstrom BR, Harrison EF, et al. Clouds and the Earth's Radiant Energy System (CERES): an earth observing system experiment. Bull Am Meteorol Soc 1996;77:853–68.
[38] Doelling DR, Sun M, Nguyen LT, et al. Advances in geostationary-derived longwave fluxes for the CERES synoptic (SYN1deg) product. J Atmos Ocean Tech 2016;33:503–21.
[39] Rutan DA, Kato S, Doelling DR, et al. CERES synoptic product: methodology and validation of surface radiant flux. J Atmos Ocean Technol 2015;32:1121–43.
[40] Key J, Wang X, Liu Y, et al. The AVHRR polar pathfinder climate data records. Remote Sensing 2016;8:167.
[41] Donohoe A, Battisti DS. Atmospheric and surface contributions to planetary albedo. J Clim 2011;24:4402–18.
[42] Ricchiazzi P, Yang S, Gautier C, et al. SBDART: a research and teaching software tool for plane-parallel radiative transfer in the Earth's atmosphere. Bull Am Meteorol Soc 1998;79:2101–14.
[43] Trepte C, Minnis P, Sun-Mack S, et al. Global cloud detection for CERES Edition 4 using Terra and Aqua MODIS data. IEEE Trans Geosci Remote Sens 2019;57:9410–49.
[44] Harrop BE, Hartmann DL. The role of cloud radiative heating within the atmosphere on the high cloud amount and top-of-atmosphere cloud radiative effect. J Adv Model Earth Sy 2016;8:1391–410.
[45] Blanchard Y, Royer A, O'Neill NT, et al. Thin ice clouds in the Arctic: cloud optical depth and particle size retrieved from ground-based thermal infrared radiometry. Atmos Meas Tech 2017;10:2129–47.
[46] Marín MJ, Serrano D, Utrillas MP, et al. Effective cloud optical depth and enhancement effects for broken liquid water clouds in Valencia (Spain). Atmos Res 2017;195:1–8.
[47] Song Z, Liang S, Zhou H. Top-of-atmosphere clear-sky albedo estimation over ocean: preliminary framework for MODIS. IEEE Trans Geosci Remote 2022;60:1–9.
[48] Qin Y, Steven ADL, Schroeder T, et al. Cloud cover in the Australian region: development and validation of a cloud masking, classification and optical depth retrieval algorithm for the advanced Himawari imager. Front Env Sci-Switz 2019;7:20.
[49] Zhan C, Liang S. Improved estimation of the global top-of-atmosphere albedo from AVHRR data. Remote Sens Environ 2022;269:112836.
[50] Zelinka MD, Myers TA, McCoy DT, et al. Causes of higher climate sensitivity in CMIP6 models. Geophys Res Lett 2020;47:e2019GL085782.
[51] Yang J, Peltier W, Hu Y. The initiation of modern "soft snowball" and "hard snowball" climates in CCSM3. Part I: the influences of solar luminosity, CO_2 concentration, and the sea ice/snow albedo parameterization. J Clim 2012;25:2711–36.
[52] Feulner G, Hallmann C, Kienert H. Snowball cooling after algal rise. Nat Geosci 2015;8:659–62.
[53] Liu Y, Yang J, Bao H, et al. Large equatorial seasonal cycle during Marinoan snowball Earth. Sci Adv 2020;6:eaay2471.
[54] Goosse H, Kay JE, Armour KC, et al. Quantifying climate feedbacks in polar regions. Nat Commun 2018;9:1913–9.
[55] Kay JE, L'Ecuyer T. Observational constraints on Arctic Ocean clouds and radiative fluxes during the early 21st century. J Geophys Res-Atmos 2013;118:7219–36.
[56] IPCC. Climate Change 2021: The Physical Science Basis. Contribution of Working Group I to the Sixth Assessment Report of the Intergovernmental Panel on Climate Change. Cambridge: Cambridge University Press; 2021.
[57] Bony S, Stevens B, Frierson DMW, et al. Clouds, circulation and climate sensitivity. Nat Geosci 2015;8:261–8.
[58] Mishra MK, Singh R, Vadnathani R, et al. Impact of vegetation greening on TOA clear-sky shortwave radiation in Northwest India. Clim Dyn 2024;62:9391–402.